

# Design of a Nondestructive 2-in-1 Instrument for Measuring Polarization and Energy Spectrum at X-ray FEL Facility

**Qingmin Zhang,<sup>a</sup> Bangjie Deng,<sup>a,1</sup> Yuanmiaoliang Chen,<sup>a</sup> Bochao Liu,<sup>a</sup> Shaofei Chen,<sup>a</sup> Jinquan Fan,<sup>a</sup> Lie Feng,<sup>b</sup> Haixiao Deng,<sup>b,2</sup> Bo Liu,<sup>b</sup> Dong Wang,**

<sup>a</sup>*Xi'an Jiaotong University,  
Xi'an, 710049, China*

<sup>b</sup>*Shanghai Institute of Applied physics, Chinese Academy of Sciences,  
Shanghai, 201800, China*

*E-mail:* [dengbangjie@foxmail.com](mailto:dengbangjie@foxmail.com), [denghaixiao@sinap.ac.cn](mailto:denghaixiao@sinap.ac.cn)

**ABSTRACT:** The Free Electron Laser (FEL), as the new generation light source, is an attractive tool in scientific frontier research, because of its advantages of full coherence, ultra-short pulse and controllable polarization. Owing to the demand of realtime bunch diagnosis during FEL experiment, it prefers a precise non-destructive measurements of polarization and X-ray energy spectrum using one instrument. In this paper, such an instrument based on the electron Time-of-Flight (e-TOF) technique was proposed. Considering the complexity and non-linearity, a numerical model in the framework of Geant4 has been developed for optimization. Taking the Shanghai Soft X-ray FEL user facility as an example, its measurement performances' dependencies on the critical parameters were studied systematically, and finally an optimal design has been obtained, achieving a resolution of 0.5% in polarization degree and 0.3 eV in X-ray energy spectrum.

**KEYWORDS:** X-ray FEL, e-TOF, Polarization, Energy spectrum

**ARXIV EPRINT:** [1702.06652](https://arxiv.org/abs/1702.06652)

---

<sup>1</sup>Corresponding author.

<sup>2</sup>Corresponding author.

---

## Contents

<b>1</b>	<b>Introduction</b>	<b>1</b>
<b>2</b>	<b>Method Description</b>	<b>2</b>
2.1	Polarization Measurement	2
2.2	$E_{ph}$ spectrum measurement	3
<b>3</b>	<b>Overall design</b>	<b>3</b>
<b>4</b>	<b>Numerical Modeling</b>	<b>6</b>
4.1	Model Description	6
4.2	Simulation	7
<b>5</b>	<b>Dependence analysis</b>	<b>8</b>
5.1	Polarization Measurement	8
5.2	$E_{ph}$ spectrum measurement	11
<b>6</b>	<b>Conclusion and discussion</b>	<b>13</b>

---

## 1 Introduction

Recently, due to their irreplaceable advantages of high brightness[1], fully transverse coherence[2, 3], ultra-short pulse duration[4] and well-defined polarization[5–7], several soft and hard X-ray FEL user facilities, as the next generation of light source, have been designed, under construction or in operation, such as LCLS (SLAC, USA)[8], SACLAC (SPRING8, Japan)[9], European XFEL (Hamburg, Germany)[10], FERMI (Trieste, Italy)[11] and SXFEL (Shanghai, China)[12]. Currently, SXFEL with designed wavelength of  $8.8\text{ nm}$  is under commissioning as a FEL test facility. Furthermore, a project upgrading SXFEL to a user facility has been launched, in which the electron beam’s energy will be boosted from  $0.84\text{ GeV}$  to  $1.6\text{ GeV}$ , in order to cover the water window or even the magnetic window[13]. According to the baseline design of SXFEL user facility, each X-ray pulse contains more than  $10^{12}$  photons with around  $100\text{ fs}$  pulse duration and controllable polarization[12].

It’s well known that high-resolution measurement of polarization properties and X-ray energy spectrum are strongly demanded in the soft X-ray magnetic circular dichroism and spectroscopy. Meanwhile, SXFEL user facility requires precise and non-invasive diagnoses of polarization and  $E_{ph}$  with  $0.5\%$  and  $0.5\text{ eV}$  in precision, respectively. However, conventional optical methods, such as transmission polarizers or multi-layer reflectors[14], are no more suitable due to soft X-ray’s strong absorption in the interaction materials. At FERMI, with X-ray energy range from  $22.9\text{ eV}$  to  $47.6\text{ eV}$ , FEL’s polarization state was measured by three methods: EUV light’s fluorescence, VUV optics and angular distribution of the photo-electrons[15]. Since electron Time-of-Flight (e-TOF) technique is utilized, the last method is routinely called as “e-TOF based”. It is a non-invasive method because only a little fraction of photons interact with the rarefied gas in e-TOF instrument and the others go through without any change. However, high resolution could be achieved due to high intensity of the beam. On the contrary, the other two methods have more serious impact on the photon

beam due to their transmission optics and phase retarders[15]. Besides, the e-TOF based instruments have been successfully applied in a polarization monitor in X-ray FEL[6, 7]. It's worth mentioning that the e-TOF based X-ray spectroscopy has been applied widely for many years, which have improved time resolution from picoseconds[16–18] to femtoseconds[19–21] and paved a road to precisely measure photon energy spectrum for ultra-short X-ray FEL pulse.

Accordingly, the e-TOF based method is able to be utilized to simultaneously measure polarization and energy spectrum of soft X-ray FEL. In this paper, Considering the complexity and non-linearity, a numerical model in the framework of Geant4[22] was established for simulating such an 2-in-1 instrument, which is based on e-TOF technique for measuring polarization and energy spectrum in the same time. Taking SXFEL user facility as an example, its systematic design and optimization was performed. Finally, our study shows that a resolution of 0.5% in polarization degree and 0.3 eV in X-ray energy spectrum can be obtained with the optimal design.

## 2 Method Description

For each pulse, X-ray photons photo-ionize target atoms and produce photo-electrons. By measuring their angular distribution and drift time, it is capable of simultaneously measuring polarization properties and  $E_{ph}$  spectrum of X-ray FEL. In this section, measurement principles will be described in details.

### 2.1 Polarization Measurement

The electric vector ( $\vec{E}$ ) of a completely polarized light could be expressed as

$$\vec{E} = A_x \cos \omega t \cdot \vec{e}_x + A_y \cdot \cos(\omega t + \Delta\varphi) \cdot \vec{e}_y \quad (2.1)$$

and it could be rewritten in the form as

$$\begin{aligned} \vec{E} = & \underbrace{(A_x + A_y \sin \Delta\varphi) \cos(\omega t) \cdot \vec{e}_x + A_y \cos \Delta\varphi \cos(\omega t) \cdot \vec{e}_y}_{\text{linear polarized part}} \\ & + \underbrace{(-A_y \sin \Delta\varphi) \cdot [\cos(\omega t) \cdot \vec{e}_x + \sin(\omega t) \cdot \vec{e}_y]}_{\text{circular polarized part}} \end{aligned} \quad (2.2)$$

As shown in Eq. 2.2, a completely polarized light could be superposed by linear polarized light ( $E_{lin}$ ) and circular polarized light ( $E_{cir}$ ), which means linear polarized light and circular polarized light could be used to describe the polarization properties of a completely polarized light. As photo-electrons' angular distribution of linear polarized photons is different from that of circular/non-polarized photons and polarization properties of FEL could be inferred by photo-electrons' angular distribution.

For  $s$  shells, the photo-electrons' angular distribution in the plane perpendicular to photons' momentum direction (Detection Plane) is described precisely enough by dipole approximation[23–25]. For linear polarized photons, the differential cross-section is

$$\left( \frac{d\sigma_i}{d\Omega} \right)_{lin} = \frac{\sigma_i}{4\pi} \left\{ 1 + \frac{\beta}{4} [3 \cos(2\theta) + 1] \right\} \quad (2.3)$$

where  $\theta$  is the angle between the photo-electrons momentum and polarization direction, and  $\beta$  is the dipole parameter related to the species of gas target. For circular/non-polarized photons, it could be

$$\left( \frac{d\sigma_i}{d\Omega} \right)_{cir} = \frac{\sigma_i}{4\pi} \left( 1 + \frac{\beta}{4} \right) \quad (2.4)$$

But for **p** shells, the differential photo-electric cross-section cannot be described by electric dipole approximation, which results in complexity for data analysis. However, electrons from **p** shells could be excluded by time of flight, due to their lower electron's kinetic energy.

Therefore, for completely polarized X-ray FEL, a normalized probability distribution of photo-electrons from **s** shells in the plane perpendicular to the photon direction is[6, 15]

$$p(\theta) = \frac{1}{2\pi} + P_{lin} \cdot \frac{3\beta}{2\pi(4+\beta)} \cos [2(\theta - \Psi)] \quad (2.5)$$

where  $P_{lin}$  linear polarization degree, and  $\Psi$  is polarization angle of linear polarized photons.

According to Eq. 2.5,  $p(\theta)$  could be obtained by fitting electrons' angular distribution with  $p(\theta) = A + B \cdot \cos [2(\theta - C)]$ . Then, linear (circular) polarization degree  $P_{lin}$  ( $P_{cir}$ ) could be

$$\left\{ \begin{array}{l} P_{lin} = \frac{B}{A} \cdot \frac{3\beta}{4+\beta} \\ P_{cir} = \sqrt{1 - P_{lin}^2} \end{array} \right. \quad (2.6)$$

$$(2.7)$$

and polarization angle could be  $\Psi = C$ .

## 2.2 $E_{ph}$ spectrum measurement

On the other hand, photons' energy could also be derived by the time of flight, since the relation between photo-electrons' energy ( $E_e$ ) and photons' energy ( $E_{ph}$ ) is

$$E_{ph} = E_e + E_b \quad (2.8)$$

where  $E_b$  represents the electrons' binding energy of a given shell, which vary with gases[26, 27]. By measuring electrons' flight time for a specified drift length  $L$ ,  $E_{ph}$  could be

$$E_{ph} = \frac{m_e L^2}{2\Delta t^2} + E_b \quad (2.9)$$

where  $\Delta t$  is the flight time of photo-electrons and  $m_e$  is the electron's rest mass.

As mentioned above,  $E_b$  varies with target gases. However, because angular distribution of Auger electrons is different from that of photo-electrons ( $E_{k,ph}$ ), the gas selection should avoid overlap with the kinetic energy of Auger electrons ( $E_{k,Auger}$ ), which is

$$E_{k,Auger} = E_i - E_j - E_k, \quad (2.10)$$

where  $E_i$ ,  $E_j$  and  $E_k$  represent electrons' binding energy of shell  $i$ ,  $j$  and  $k$ , respectively. These properties could be found in references [25] and [28].

Making use of pulse waveform analysis and earliest arrival time measurement, the flight time spectrum for photo-electrons could be obtained, from which  $E_{ph}$  spectrum could be derived according to Eq. 2.9.

## 3 Overall design

According to physical principles described above, photo-electrons' angular distribution could be measured by placing detectors in the Detection Plane and their energy spectrum could be obtained by the time of flight. The instrument is designed to contain three subsystems: detector, electronics and data analysis, as demonstrated in Fig. 1.

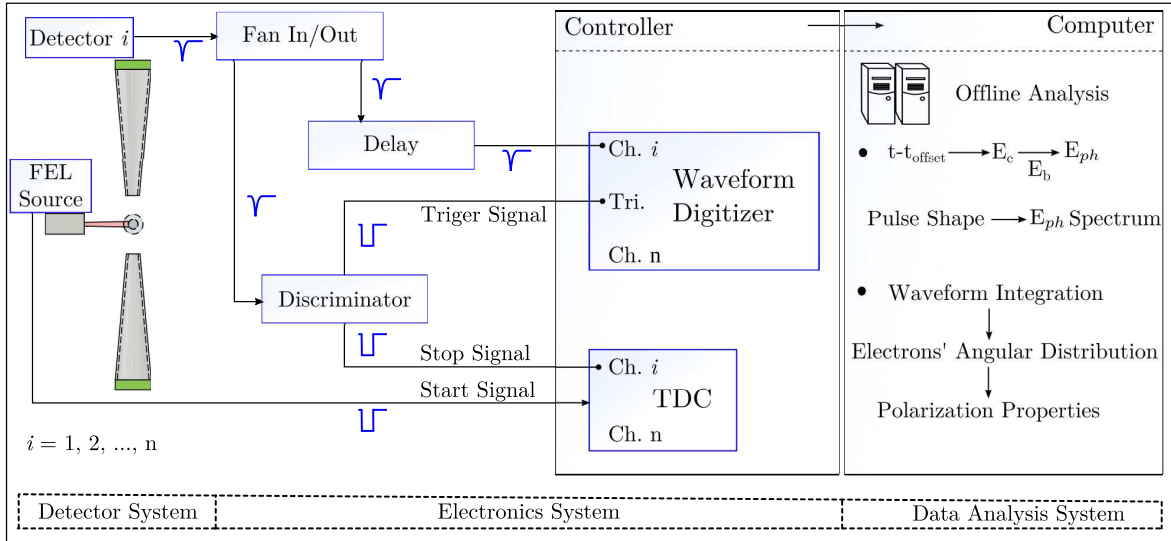


**Figure 1.** The framework of the instrument.

The detector system is composed of differential vacuum system and a given number of identical e-TOF detectors for photo-electrons' generation, drifting and detection. Gas target is located at the center of the instrument for photo-electric reaction, being uniformly surrounded by e-TOF detectors. Each e-TOF detector is an electron multiplier equipped with a collimation tube. The Micro-Channel Plate (MCP) is preferred as electron multiplier due to its timing resolution of hundreds picoseconds, better response linearity because of its numerous independent micro channels and the electrons' dispersive arrival at MCP in space. Besides, circular truncated cone collimation tubes were designed for a better placement. Following X-ray FEL beam's arrival, photo-electrons generate in central volume, drift through the collimation tubes and are detected by electron detectors finally. Considering statistical errors, central volume should be in a fairly high pressure for generating enough photo-electrons, while its surrounding volume should be in very low pressure to minimize electrons' loss and scattering during electrons' drift, and to satisfy detectors' working pressure requirement. Accordingly, differential vacuum system (DVS) was adopted. Besides, small difference between target gas and drifting environment is preferable to avoid complicated design of DVS.

The electronics system was designed to record the flight time and signal waveform of photo-electrons by using Time-to-Digital Converter (TDC) unit and Waveform Digitizer for all detectors. For each pulse, TDC is triggered by a start signal supplied by timing system of FEL source, and stopped by a signal from a discriminator. In the meanwhile, the stop signal is also transferred into the Waveform Digitizer for signal shape recording. A proper delay for the detection signal transferred into Waveform Digitizer is introduced for synchronization in order to record the signal shape completely. Besides, the signal shape could be integrated to obtain signal charge, which is proportional to the number of photo-electrons. Then, photo-electrons' angular distribution is obtained to conclude the polarization properties. Combining the signal shape and flight time, photo-electrons' flight time spectrum could be determined.

The data analysis system was designed to analyze waveform time series data, from which photo-electrons' flight time spectrum could be derived by using pulse shape analysis methods. Furthermore,  $E_{ph}$  spectrum could be obtained according to Eq. 2.9 after an offset time correction. It's reasonably assumed that there's no saturation effect for detector's response due to the moderate number of detected electrons, and that pulse shape

for each electron is quite same. Therefore, signal's integration charge for each channel ( $Q_i$ ,  $i = 1, 2, \dots, 16$ ) is proportional to the number of detected photo-electrons. And X-ray FEL's polarization properties ( $P_{lin}$  &  $P_{cir}$ ) could be obtained by fitting  $Q_i$  with  $p(\theta) = A + B \cos 2[(\theta + C)]$  and applying Eq. 2.6 to Eq. 2.7. Based on assumptions mentioned above, a linear model was proposed to analyze signal waveform in order to obtain the flight time spectrum. The sampled signal pulse  $P(i\Delta t_s)$ , ( $i = 1, 2, \dots, n$ ) with sampling time interval  $\Delta t_s$  could be described as Eq. 3.1.

$$P = [P_1, P_2, \dots, P_i, \dots, P_{n-1}, P_n] \quad (3.1)$$

Because  $\Delta t_s$  for Waveform Digitizer is much larger than the realistic interval of electrons' arrival time, sampled signal should be interpolated to acquire smaller time interval  $\Delta t_i$  for decomposition. The interpolation signal pulse shape  $I(j\Delta t_i)$ , ( $j = 1, 2, \dots, m$ ) could be obtained by interpolating sampled signal  $P(i\Delta t_s)$  in a small interpolation time interval  $\Delta t_i$ . Obviously,  $m \geq n$  is required and  $n\Delta t_s$  is much longer than the typical width of the whole signal. Commonly, amplitude of a single photo-electron's charge signal ( $S_{0,j}$ ) with time interval  $\Delta t_i$  in simulation at time  $t = j\Delta t_i$  ( $j = 1, 2, \dots, m$ ) could be described by Log-Normal distribution  $f(t)$  in the form of Eq. 3.2.

$$f(t) = e^{-\frac{1}{2} \left( \frac{\log(t/\tau)}{\sigma_s} \right)^2} \quad (3.2)$$

where  $\tau$  and  $\sigma_s$  defines signal's location and scale respectively[29]. Therefore, signal's pulse shape ( $\mathbf{S}_0$ ) for a single electron without delay could be described digitally as below:

$$\begin{cases} \mathbf{S}_0 = [S_{0,1}, S_{0,2}, \dots, S_{0,j}, \dots, S_{0,m}]^T \\ S_{0,j} = f(j\Delta t_i) \quad (j = 1, 2, \dots, m) \end{cases} \quad (3.3)$$

Thus, the pulse shape for single electron with a delay of  $k\Delta t_i$  ( $k = 0, 1, 2, \dots, m-1$ ) could be expressed digitally as below:

$$\begin{cases} \mathbf{S}_k = [S_{k,1}, S_{k,2}, \dots, S_{k,j}, \dots, S_{k,m}]^T \\ S_{k,j} = f((j-k)\Delta t_i) \quad (j = 1, 2, \dots, m) \end{cases} \quad (3.5)$$

$$(3.6)$$

Then, signal matrix for a series of single electrons with a delay  $k\Delta t$  could be written as

$$\mathbf{S}_{m \times m} = [\mathbf{S}_0, \mathbf{S}_1, \dots, \mathbf{S}_{m-2}, \mathbf{S}_{m-1}] \quad (3.7)$$

In addition, the number of electrons for each bin could be

$$\mathbf{C}_{m \times 1} = [C_0, C_1, \dots, C_{m-2}, C_{m-1}]^T \quad (3.8)$$

Thus,

$$\mathbf{I} = \mathbf{S} \cdot \mathbf{C} + \mathbf{e} \quad (3.9)$$

where  $\mathbf{e}$  is the error term due to noise. Therefore, the number of electrons for each timing bin is obtained by solving Eq. 3.9, and namely, electron's flight time spectrum could be obtained. A least square method is chosen for optimization in solving  $\mathbf{C}$  in Eq. 3.9. The estimated number of photo-electrons  $\hat{\mathbf{C}}$  could be obtained by various optimization algorithms with constraints ( $C_j \geq 0$ ,  $j = 1, 2, \dots, m$ ), such as the Conjugate Gradient method[30], the BFGS method[31], etc. Finally,  $E_{ph}$  Spectrum could be derived by Eq. 2.9.

## 4 Numerical Modeling

Because the instrument's performance is influenced by many factors and photo-electrons' interaction with gas cannot be well described analytically, it's impossible to optimize the design analytically. Hence, a numerical simulation model will be established in the framework of Geant4, which is a Monte Carlo nuclear physics simulation software[22]. In order to simulate polarized photons' interaction with target gas, the Livermore Polarized Physics Model with G4EMLOW-6.48 data[32] was used and a proper energy threshold of 100 eV was set for tracking all particles. Major processes in simulation were the X-ray's photoelectric process, electrons' ionization and scattering.

### 4.1 Model Description

In order to simulate the detector's physics, the detector model was established including detector construction, the corresponding physics list and particle gun for incident photons.

In numerical model, instrument's geometry was simplified appropriately, as demonstrated in Fig. 2(a). Electron multipliers and collimating tubes were set in shape of thin cylinders and hallow cone shells respectively. Critical parameters are labelled in Fig. 2(b). And an overall view of the instrument is demonstrated in Fig. 2(c).

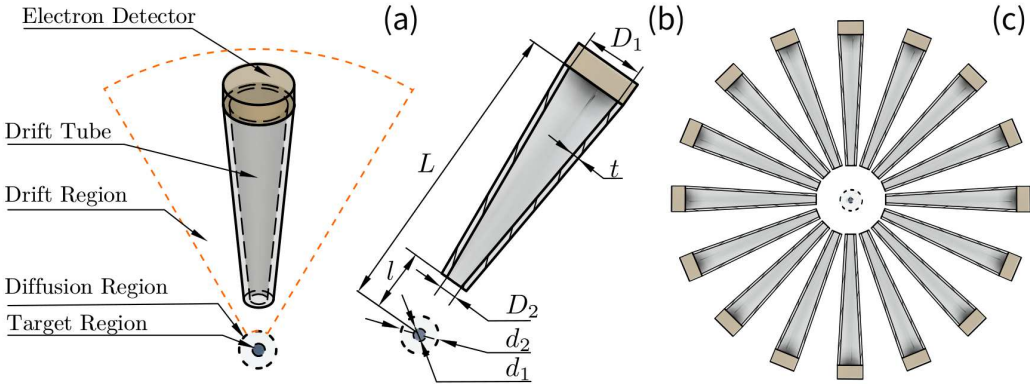


**Figure 2.** The sketch of e-TOF detectors and gas environment. (a): An e-TOF detector and gas regions of the spectrometer. (b): Critical parameters in design. (c) Overall layout view of e-TOF detectors.

The geometry of differential vacuum system was omitted and the gaseous environment was divided into three parts according to the pressure magnitude: Target Region, Diffusion Region, and Drift Region. Target region, a high-pressure cylinder region, was located at the center of instrument, where gas was injected and photo-electrons were produced. Since the FEL pulse duration is ultra short, pressure in Target Region was considered to be stable during a single pulse. Generally, the target gas with a higher  $E_b$  (such as  $O_2$ ) means a better energy resolution of  $E_{ph}$  for a given drift length. However, in order to test the model in a moderate condition,  $N_2$  ( $E_b = 403\text{eV}$ ) was adopted. Drift region, a steady low-pressure region for electrons' drifting, is to reduce electrons' scattering and to satisfy electron multipliers' working environment (pressure should be less than  $0.1\text{Pa}$ ). To simulate the pressure transition region between Target Region and Drift Region, a Diffusion Region with 16 radius bins in linear gradient pressure was adopted in numerical simulation. Additionally, the terrestrial magnetism was also considered, which was set to be perpendicular to the Detection Plane, as it bends electrons maximally for such a set-up.

The incident polarized X-ray photons were sampled according to the start-to-end FEL simulation under typical SXFEL working condition, in which FEL's average energy is around 621 eV with a narrow bandwidth of about 0.8 eV[13]. And photons' direction were set to be perpendicular to the Detection Plane. In terms of photon's polarity, completely polarized photons were simulated by combination of linear polarized light and circular light photons with a given  $P_{lin}$  (determined by FEL working condition). Linear polarized photons' polarization angle was set to be  $\Psi$ , and the  $\vec{E}_{cir}$  direction for each circular polarized photon was sampled from uniform distribution in  $[0, 2\pi]$ . Meanwhile, photon beam's transverse distribution was considered as a normal distribution. Usually, beam diameter ( $D_b$ ) was defined as the place where photon's intensity is reduced to  $1/e^2$  of its maximum[33], which was calculated as  $4\sigma$  of the Normal distribution.

## 4.2 Simulation

In simulation, variance reduction technique was introduced for improving simulation efficiency and electronics signals were digitized for processing. Details are described below and simulation results are presented.

Because there are more than  $10^{12}$  photons in a single laser pulse, a variance reduction technique of cross-section bias for only photo-electric process was adopted. Cross section for photoelectric was  $10^5$  times larger, while the other cross sections remain unchanged. Therefore, the number of total sampling events was reduced significantly, while effective events remained the same.

For each event, once photo-electrons were detected, the charge and their drift time were recorded. Detectors' simulated signals were produced according to Eq. 3.2 with proper shape parameters ( $\tau$  &  $\sigma_s$ ). The Discriminator, Fan In/Out unit, delay cables and TDC unit (measuring the earliest electron's arrival time) were omitted because e-TOF signal shape could be obtained directly in simulation. By adopting method mentioned above, the angular distribution could be derived by integration of signal shape. Meanwhile the  $E_{ph}$  spectrum was derived by pulse shape analysis.

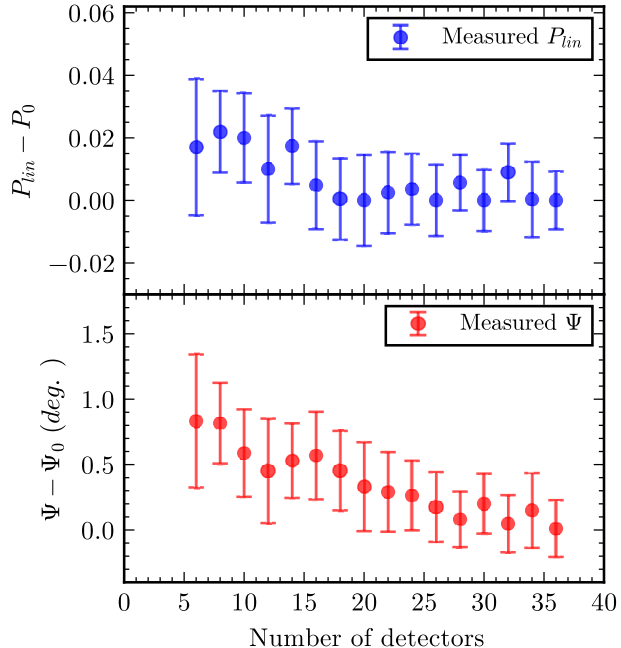


**Figure 3.** Performance of polarization measurement is a function of the number of detector

Due to terrestrial magnetism could be corrected by various methods, such as magnetic shielding and reverse magnetic field. Therefore, it was omitted in this simulation and the dependence on it will be studied later. Key parameters of baseline design are listed in Table 1. It's worth mentioning that the detectors are uniformly deployed for measuring any polarization angle and that the number of detectors is determined by balance of cost, complexity and performance dependence analysis. Because this instrument's primary goal is to measure polarization precisely, the performance of polarization measurement was analyzed by varying the number of detectors with the other baseline parameters exactly same with TABLE 1. As shown in Fig.3, it's seen that the performance improvement for polarization measurement is not sensitive to the number of detectors when the number of detector is greater than 16. Hence, the number of detectors is fixed at 16.

In addition, the performance for baseline design is shown in Fig.4, which verifies the numerical model.

**Table 1.** Critical parameters of baseline design

Parameters	Value	Descriptions
$E_{ph,av}$	621.4 eV	Average energy of a typical SXFEL pulse.
$E_{ph,band}$	0.9 eV	Bandwidth of a typical SXFEL pulse.
$N$	16	Number of Detectors
Gas	$N_2$	Target gas species.
$E_b$	403 eV	Binding energy of 1s orbit.
$d_1$	5 mm	Diameter of Target Region.
$d_2$	10 mm	Diameter of Diffusion Region.
$D_b$	0.1 mm	Average diameter of laser beam.
$L$	350 mm	Drift distance.
$l$	30 mm	Collimating tubes' offset.
$D_1$	27 mm	Diameter of electron multipliers.
$D_2$	3.24 mm	Diameter of collimation tubes' front end.
$B$	0 Gauss	Terrestrial magnetic field intensity.
$\tau$	200 ps	Location parameter of detector's response for an electron
$\sigma_s$	0.7	Scale parameter of detector's response for an electron
$t_s$	150 ps	Sampling time interval.
$t_i$	50 ps	Interpolation time interval.

## 5 Dependence analysis

Resolutions of 0.5% for polarization degree measurement and 0.5 eV for  $E_{ph}$  spectrum measurement are required by SXFEL user facility, so critical parameters' influences to polarization and  $E_{ph}$  spectrum measurements are studied in this section.

### 5.1 Polarization Measurement

Precision of polarization measurement is related to the number and angular distribution of detected photo-electrons. Potential critical factors might include gas pressure for both target region and drift region, electron's drift length, detector size and the remnant terrestrial magnetic field. In order to examine their influence, polarization measurement performance will be evaluated by the absolute deviation and standard error of  $P_{lin}$  for an incident FEL pulse with linear polarization degree  $P_0 = 1$ .

For Target Region, high gas pressure may mean a larger photo-electrons' yield and smaller statistical error term. However, in the same time, it also has a big impact to photo-electrons' drifting, resulting in non-convergent

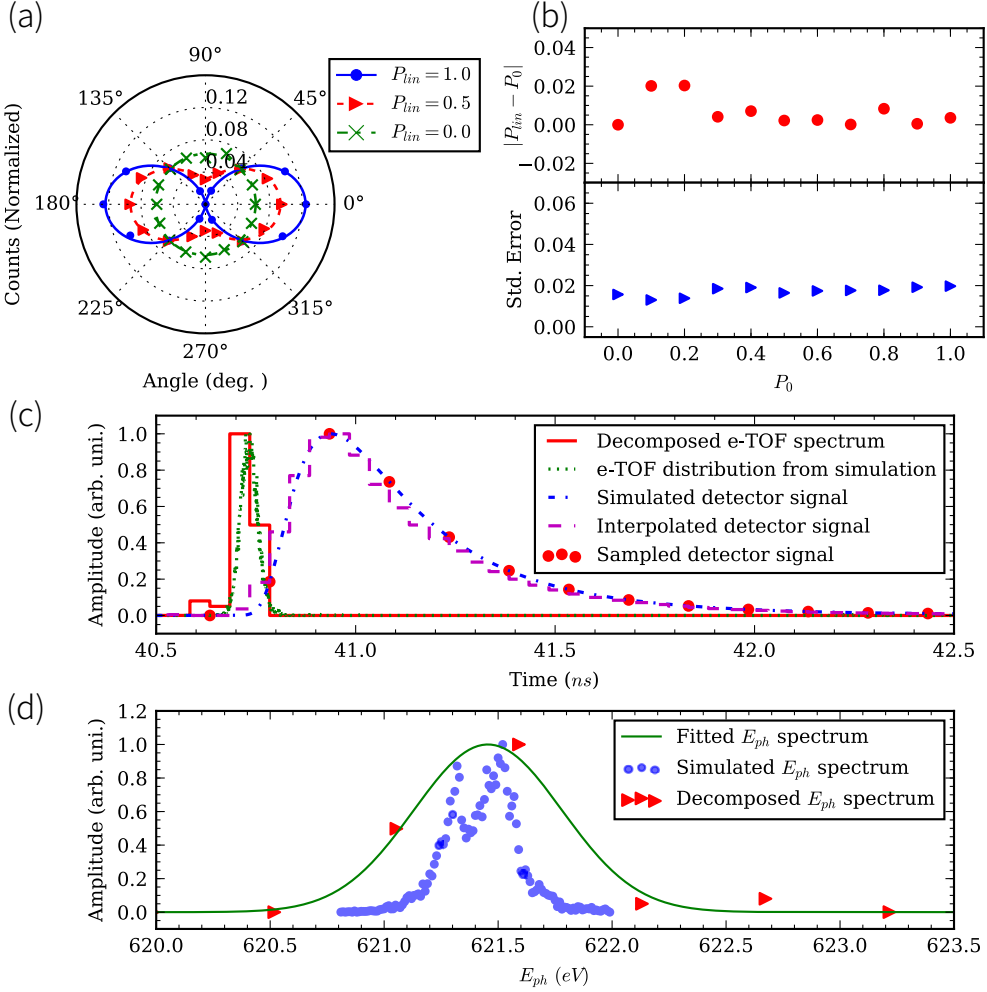


**Figure 4.** The simulation result of baseline. (a): Polarization measurement for FEL polarized in angle of zero with varied  $P_{lin}$  under polar coordinate system. (b): The absolute deviation of polarization measurement for different linear polarization fraction  $P_0$  in simulation. (c): The decomposition process of TOF signals, compared with realistic electrons' TOF distribution. Simulated e-TOF signal (dashed & dotted) was sampled by Waveform Digitizer in  $\Delta t_s = 150$  ps and interpolated with  $\Delta t_i = 50$  ps. After off-line analysis, decomposed e-TOF spectrum (solid) is capable to illustrate the outline of e-TOF distribution from simulation (dotted). (d): The comparison of decomposed energy spectrum (fitted by Normal distribution) and  $E_{ph}$  spectrum from start-to-end simulation of FEL.

measurement. Accordingly it need to be optimized and related simulation results are shown in Fig. 5, indicating an optimal  $P_t$  in the range from 0.1 Pa to 1.0 Pa.

For Drift Region, high pressure prevents photo-electrons' drifting. As shown in Fig. 6, when  $P_d$  is less than 0.1 Pa, deviations of measured  $P_{lin}$  change insignificantly and satisfy the corresponding design requirements.

Longer drift length indicates larger statistical error due to smaller acceptance angle. Inferring from Fig. 7, as drift distance increased,  $|\Delta P_{lin}|$  changes slightly. Therefore, an acceptable drift length might be from 200 mm to 400 mm, satisfying the design requirement.

Electron detectors with smaller size might lead to greater statistical error due to small acceptance angle,

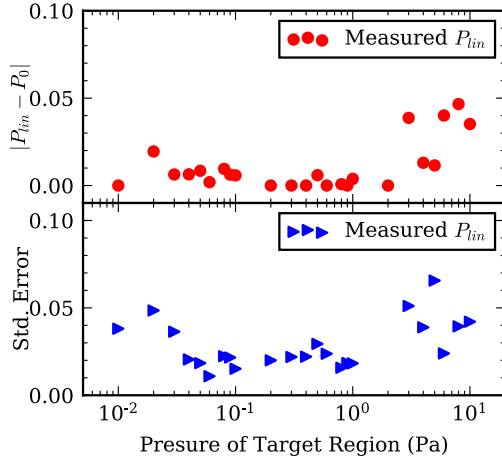


**Figure 5.** The deviation of polarization measurement with changing pressures in Target Region

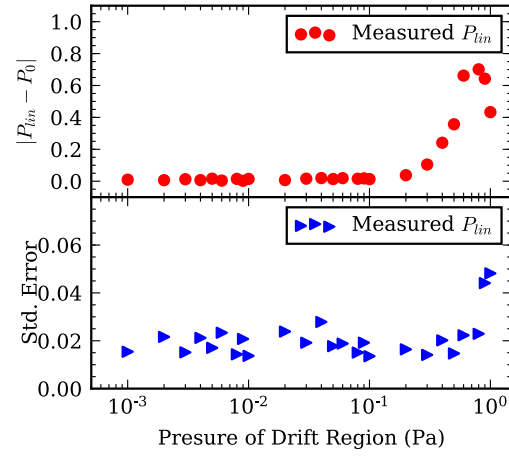


**Figure 6.** The deviation of polarization measurement with changing pressure of Drift region

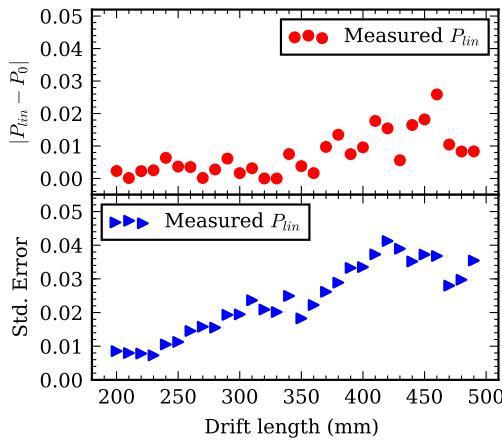


**Figure 7.** The deviation of polarization measurement with changing drift distances

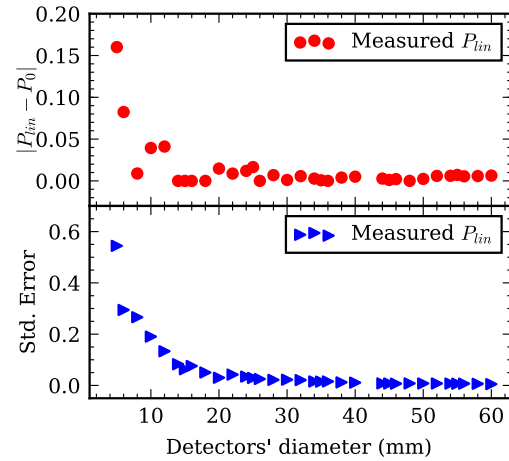


**Figure 8.** The deviation of polarization measurement with changing detector's size

while larger detectors might cause error term due to unsuitable assumption of Detection Plane and inaccurate positioning. The result is demonstrated in Fig. 8. From the result, detected photon-electrons could be regarded as a point source and to be within the Detection Plane when detectors' diameter ( $D_2$ ) is in the range from 5 mm to 60 mm and drift length  $L$  is 350 mm. Meanwhile,  $D_2$  should be larger than 30mm (typically 42mm for commercial products) to cater for design requirement.

Terrestrial magnetic field bends photo-electrons' drift path, resulting in deviations for measurement. Such deviations could be avoided by magnetism shielding or reversed magnetic field, however how weak the residual magnetic field should be is a question to be answered by us. Under the circumstance that magnetic field is

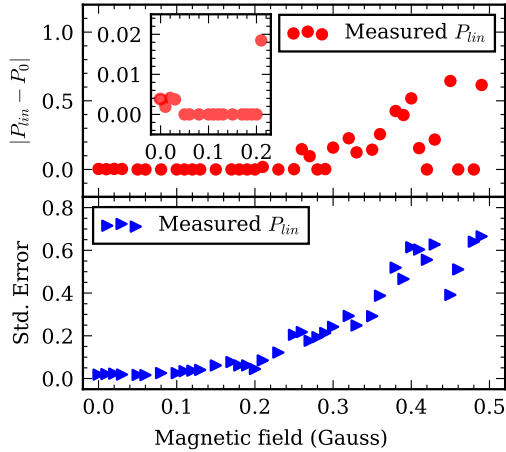


**Figure 9.** The deviation of polarization measurement with changing residual earth magnetic field

parallel to the laser beam line and perpendicular to the plane of e-TOF detectors, the magnetic field bends the photo-electrons maximum, so the dependence of polarization measurement on remnant terrestrial magnetism was studied under this situation. As shown in Fig. 9, it suggests that a maximum residual magnetic field around 0.2 Gauss could be neglected and that the design requirement could be met.

### 5.2 $E_{ph}$ spectrum measurement

$E_{ph}$  spectrum measurement prefers longer signal duration and smaller sampling/interpolation time interval, both of which means higher resolution. Longer signal duration could be achieved by longer drift length ( $L$ ) and target gas with higher binding energy. Sampling time interval  $\Delta t_s$  is often determined by the maximum sampling rate of Waveform Digitizer. Large  $\Delta t_s$  could result in interpolated signal's distortion. Besides, interpolation time interval  $\Delta t_i$  should be chosen according to the FWHM, because two overlapped signal peak could be mistaken as one peak. In the following, key parameters: species of target gas, drift length  $L$ , and sampling & interpolation time interval ( $\Delta t_s$  &  $\Delta t_i$ ) are studied. In order to examine performance of measuring  $E_{ph}$  spectrum, primary X-ray's energy in Normal distribution with  $\mu = 621 \text{ eV}$  (average) and  $\sigma = 0.1 \text{ eV}$  (deviation) was simulated. The estimated parameters ( $\hat{\mu}$  and  $\hat{\sigma}$ ) could be obtained by fitting decomposed signal with normal distribution. Since  $\hat{\mu}$  could be corrected by other advanced spectrometer,  $\hat{\sigma} - \sigma$  might be the figure of merit (FOM) for evaluating the spectrometer's performance.

According to Eq. 2.8, target gas with higher binding energy means smaller photo-electrons' energy, longer signal's duration for a given drift length, and furthermore a higher resolution when other parameters remain. Both Nitrogen and Oxygen are acceptable and their binding energies are about 403 eV and 540.43 eV respectively [26]. The result of  $E_{ph}$  spectrum measurement simulations for these two kinds of target gas are demonstrated in Fig. 10. According to the simulation,  $\hat{\sigma}$  of  $O_2$  is much smaller than that of  $N_2$ . Therefore,  $O_2$  is more suitable for  $E_{ph}$  spectrum measurement.

Longer drift length converts tiny energy difference of electrons into measurable time and helps to extend signal duration for Digitizers' sampling. Simulation result for the dependence analysis of drift distance  $L$  is reported in Fig. 11. From the result, it could be inferred that  $L$  should be at least 350 mm for  $N_2$ . But for  $O_2$  target, the smallest deviation of  $\hat{\sigma}$  is located at  $L$  around 400 mm, which could be understood because long drift length means fewer detected photo-electrons while short drift length results in short flight time. In short,  $O_2$

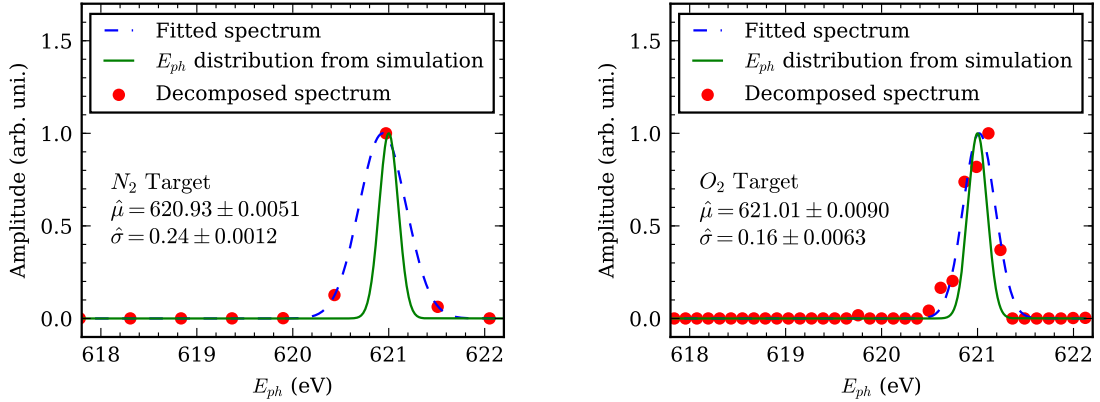


**Figure 10.** Simulation result for  $N_2$  target (left) and  $O_2$  target (right) with the sampling time interval  $\Delta t_s = 100$  ( $ps$ ) and re-sampling time interval  $\Delta t_i = 50$  ( $ps$ ).

target is more suitable than  $N_2$  and  $L = 400$   $mm$  for  $O_2$  target is the optimal design.

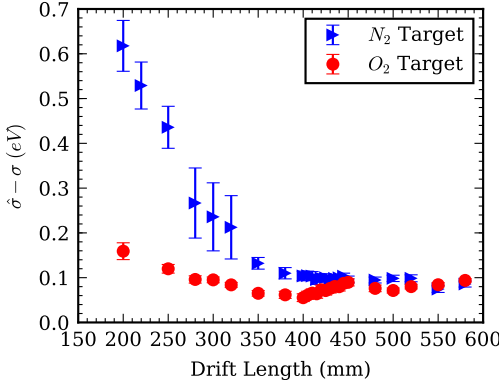


**Figure 11.** The deviation of  $\hat{\sigma}$  with changing drift distances

Nowadays, sampling rate for ADC has been up to 30  $Gs$ [34]. Generally,  $t_s$  from 50  $ps$  to 400  $ps$  is practicable and acceptable. By changing  $\Delta t_s$  and  $\Delta t_i$ , the variation of  $\hat{\sigma}$  are demonstrated in Fig. 12 and Fig. 13. According to Fig. 12 and Fig. 13,  $\hat{\sigma}$  with  $O_2$  target is better than that of  $N_2$  when both  $\Delta t_s$  and  $\Delta t_i$  are same. Besides, for  $O_2$  target, the design requirement could be satisfied as long as  $\Delta t_s$  and  $\Delta t_i$  are within the simulation range ( $\Delta t_i < \Delta t_s$  is required).

In addition, the same method for energy spectrum reconstruction was used to separate photons with 2 energies from the same X-ray FEL pulse under the optimized conditions ( $E_{ph1} = 621$   $eV$ ,  $E_{ph2} = 621$   $eV + \Delta E$ ,  $\Delta t_s = 150$   $ps$ ,  $O_2$  target). The scan was performed by changing  $\Delta E$  and that two energy peaks were obvious when  $\Delta E \geq 0.3$   $eV$ , giving an energy resolution of 0.3  $eV$

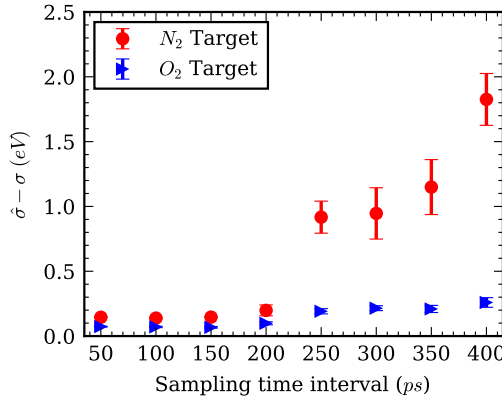


**Figure 12.** The deviation of  $\hat{\sigma}$  with changing sampling time interval  $\Delta t_s$

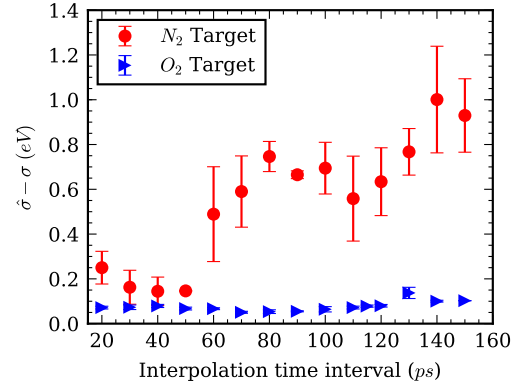


**Figure 13.** The deviation of  $\hat{\sigma}$  with changing interpolation time interval  $\Delta t_i$

## 6 Conclusion and discussion

Based on the numerical optimization above, we have validated its feasibility for e-TOF based polarimeter and spectrometer for a X-ray FEL user facility. The polarization resolution is 0.5% and the photon's energy resolution is 0.3 eV for the optimized design:

1. Target Region's pressure is in the range from 0.1 Pa to 1.0 Pa and Drift Region's pressure is below 0.1 Pa;
2. Drift distance  $L$  is longer than 400 mm;
3. Detectors' diameter is larger than 30 mm;
4. Remnant magnetic field should be controlled to be less than 0.2 Gauss;
5. Sampling time interval is in the range from 50 ps to 400 ps and interpolation time interval is in the range from 20 ps to 140 ps.

There are still a few conditions to be considered for further study, such as the inference of  $P_{lin}$  with photo-electrons from **p** sub-shells and the inferior influence of Auger electrons to the polarity measurement.

## Acknowledgments

This work is supported by the Fundamental Research Funds for the Central Universities (Grant No. xjj2017109), Natural Science Fundamental Research Plan of Shaanxi Province (Grant No. 2016JM1019), China Association for Science and Technology, and Ten Thousand Talents Program.

## References

[1] B. W. J. McNeil and N. R. Thompson, *X-ray free-electron lasers*, *Nature Photonics* **4** (2010) 814–821.

[2] A. Singer, I. A. Vartanyants, M. Kuhlmann, S. Duesterer, R. Treusch and J. Feldhaus, *Transverse-coherence properties of the free-electron-laser FLASH at DESY*, *Physical Review Letters* **101** (2008) 2–5.

[3] F.-e. L. Saclà, X.-r. Regime and F. Lehmkö, *Single Shot Coherence Properties of the Free-Electron Laser SACLA in the Hard X-ray Regime*, .

[4] C. Behrens, F.-J. Decker, Y. Ding, V. A. Dolgashev, J. Frisch, Z. Huang et al., *Few-femtosecond time-resolved measurements of X-ray free-electron lasers*, *Nature Communications* **5** (apr, 2014) 1–7.

[5] H. Deng, T. Zhang, L. Feng, C. Feng, B. Liu, X. Wang et al., *Polarization switching demonstration using crossed-planar undulators in a seeded free-electron laser*, *Physical Review Special Topics - Accelerators and Beams* **17** (feb, 2014) 020704.

[6] E. Allaria, B. Diviacco, C. Callegari, P. Finetti, B. Mahieu, J. Viefhaus et al., *Control of the polarization of a vacuum-ultraviolet, high-gain, free-electron laser*, *Physical Review X* **4** (2014) .

[7] A. A. Lutman, J. P. MacArthur, M. Ilchen, A. O. Lindahl, J. Buck, R. N. Coffee et al., *Polarization control in an X-ray free-electron laser*, *Nature Photonics* **10** (jul, 2016) 468–472.

[8] EmmaP., AkreR., ArthurJ., BiontaR., BostedtC., BozekJ. et al., *First lasing and operation of an angstrom-wavelength free-electron laser*, *Nature Photonics* **4** (sep, 2010) 641–647.

[9] T. Ishikawa, H. Aoyagi, T. Asaka, Y. Asano, N. Azumi, T. Bizen et al., *A compact X-ray free-electron laser emitting in the sub-angstrom region*, *Nature Photonics* **6** (aug, 2012) 540–544.

[10] A.S.Schwarz and European XFEL Group, *the European X-Ray Free Electron Laser Project At Desy*, *Proc. 2004 FEL Conf.* (2004) 85.

[11] R. P. Walker, D. Bulfone, F. Cargnello, M. Castellano, F. Cevenini, F. Ciocci et al., *The FERMI FEL project at Trieste*, *Nuclear Instruments and Methods in Physics Research, Section A: Accelerators, Spectrometers, Detectors and Associated Equipment* **375** (1996) 19–22.

[12] Z. T. Zhao, S. Y. Chen, L. H. Yu, C. X. Tang, L. X. Yin, D. Wang et al., *SHANGHAI SOFT X-RAY FREE ELECTRON LASER TEST FACILITY*, in *IPAC*, (San Sebastián, Spain), pp. 3011–3013, 2011.

[13] M.-H. Song, C. Feng, D.-Z. Huang, H.-X. Deng, B. Liu and D. Wang, *Wakefields studies for the sxfel user facility*, *Nuclear Science and Techniques* **28** (May, 2017) 90.

[14] L. Feng, H. Deng, T. Zhang, C. Feng, J. Chen, X. Wang et al., *Single-shot measurement of free-electron laser polarization at SDUV-FEL*, *Chinese Physics C* **39** (2015) 028101.

[15] P. Finetti, M. Zangrando, G. D. Ninno, J. Buck, C. Svetina, S. D. Mitri et al., *Polarization measurement of free electron laser pulses in the vuv generated by the variable polarization source fermi*, *Proceedings of SPIE - The International Society for Optical Engineering* **9210** (2014) 273–274.

[16] A. J. Nelson, J. Dunn, T. Van Buuren and J. Hunter, *X-ray laser-induced photoelectron spectroscopy for single-state measurements*, *Applied Physics Letters* **85** (2004) 6290–6292.

[17] M. Saes, F. van Mourik, W. Gawelda, M. Kaiser, M. Chergui, C. Bressler et al., *A setup for ultrafast time-resolved x-ray absorption spectroscopy*, *Review of Scientific Instruments* **75** (2004) .

[18] A. M. March, A. Stickrath, G. Doumy, E. P. Kanter, B. Krässig, S. H. Southworth et al., *Development of high-repetition-rate laser pump/x-ray probe methodologies for synchrotron facilities*, *Review of Scientific Instruments* **82** (2011) .

[19] R. W. Schoenlein, S. Chattopadhyay, H. H. W. Chong, T. E. Glover, P. A. Heimann, C. V. Shank et al., *Generation of Femtosecond Pulses of Synchrotron Radiation*, *Science* **287** (2000) 2237–2240.

[20] X. Zhang, G. Smolentsev, J. Guo, K. Attenkofer, C. Kurtz, G. Jennings et al., *Visualizing Interfacial Charge Transfer in Ru-Dye-Sensitized TiO<sub>2</sub> Nanoparticles Using X-ray Transient Absorption Spectroscopy*, *The Journal of Physical Chemistry Letters* **2** (mar, 2011) 628–632.

[21] C. Bressler, C. Milne, V.-T. Pham, A. ElNahhas, R. M. van der Veen, W. Gawelda et al., *Femtosecond XANES Study of the Light-Induced Spin Crossover Dynamics in an Iron(II) Complex*, *Science* **323** (2009) 489–492.

[22] S. Agostinelli, J. Allison, K. Amako, J. Apostolakis, H. Araujo, P. Arce et al., *Geant4* simulation toolkit, *Nuclear Instruments and Methods in Physics Research Section A: Accelerators, Spectrometers, Detectors and Associated Equipment* **506** (2003) 250–300.

[23] J. W. Cooper, *Photoelectron-angular-distribution parameters for rare-gas subshells*, *Physical Review A* **47** (1993) 1841–1851.

[24] S. T. Manson and A. F. Starace, *Photoelectron angular distributions: energy dependence for s subshells for s subshells*, *Reviews of Modern Physics* **54** (1982) 389–405.

[25] A. Paulus, C. Winterfeldt, T. Pfeifer, D. Walter, G. Gerber and C. Spielmann, *Novel time-of-flight electron spectrometer optimized for time-resolved soft-x-ray photoelectron spectroscopy*, *Review of Scientific Instruments* **77** (2006) 0–6.

[26] M. B. Trzhaskovskaya, V. G. Yarzhemsky and V. I. Nefedov, *Photoelectron angular distribution parameters for elements z=1 to z=54 in the photoelectron energy range 100Å–5000 ev*, *Atomic Data and Nuclear Data Tables* **77** (jan, 2001) 97–159.

[27] M. Trzhaskovskaya, V. Nefedov and V. Yarzhemsky, *Photoelectron angular distribution parameters for elements z=55 to z=100 in the photoelectron energy range 100–5000 ev*, *Atomic Data and Nuclear Data Tables* **82** (2002) 257–311.

[28] M. Yamazaki, J.-I. Adachi, T. Teramoto and A. Yagishita, *Experimental evidence of interatomic resonant Auger electron emission from fixed-in-space NO molecules*, *Journal of Physics B: Atomic, Molecular and Optical Physics* **40** (2007) 207–213.

[29] S. Jetter, D. Dwyer, W.-Q. Jiang, D.-W. Liu, Y.-F. Wang, Z.-M. Wang et al., *PMT waveform modeling at the Daya Bay experiment*, *Chinese Physics C* **36** (2012) 733–741.

[30] M. R. Hestenes and E. Stiefel, *Methods of conjugate gradients for solving linear systems*, *Journal of Research of the National Bureau of Standards* **49** (1952) 409–436, [[1102.0183](#)].

[31] D. C. Liu and J. Nocedal, *On the limited memory BFGS method for large scale optimization*, *Mathematical Programming* **45** (aug, 1989) 503–528.

[32] C. Champion, S. Incerti, H. Aouchiche and D. Oubaziz, *A free-parameter theoretical model for describing the electron elastic scattering in water in the Geant4 toolkit*, *Radiation Physics and Chemistry* **78** (2009) 745–750.

[33] A. E. Siegman, *How to (maybe) measure laser beam quality*, in *DPSS (Diode Pumped Solid State) Lasers: Applications and Issues*, p. 6, Optical Society of America, 1998. [DOI](#).

[34] X. Zhu, D. Wu, L. Zhou, Y. Huang, J. Wu and X. Liu, *A four-channel time-interleaved 30-gs/s 6-bit adc in 0.18  $\mu$ m sige bicos technology*, *Science China Information Sciences* **60** (2017) 129401.